ORIGINAL ARTICLE

Seismic site–city interaction analysis of super-tall buildings surrounding an underground station: a case study in Hong Kong

Bence Kato[1,2] · Gang Wang[2]

Abstract

Understanding site–city interaction (SCI) is important for sustainable urban development in seismic regions. Due to vertical expansion of cities, super-tall buildings with deep foundations and large underground chambers are often simultaneously present. However, the role of these structures and their layouts in SCI have not been considered before. This study quantifies the effects of SCI at a congested transport hub in Hong Kong, utilizing 3D numerical modeling. At the site, 16 high-rise buildings surround a center plaza with a large metro station underground. This research demonstrates that the building layout, building inertia, and interaction between underground structures through the soil govern SCI at the site, causing ground motion perturbations and wave trapping between buildings. The presence of buildings causes up to 150–200% amplification in the short-period acceleration spectra and 150% PGA amplifications in the center plaza. Notable SCI effects on structures only appear as excess maximum story accelerations, in the order of $1-2\,\mathrm{m/s^2}$, and increased destructive kinetic energy. Amid and around the high-rise buildings, SCI effects may significantly increase seismic demand on short structures. Finally, increasing the seismic demand for the design of super-tall and low-rise buildings is recommended to account for the SCI effects.

Keywords Site–City Interaction · Spectral element simulation · Super-tall buildings · Underground structure

✉ Gang Wang
gwang@ust.hk

Bence Kato
bkato@ust.hk

1 Department of Civil and Environmental Engineering, Harbin Institute of Technology (Shenzhen), Shenzhen, China

2 Department of Civil and Environmental Engineering, Hong Kong University of Science and Technology, Clear Water Bay, Kowloon, Hong Kong SAR, China

1 Introduction

Ground motion estimation and resilient seismic design of structures have been at the forefront of earthquake engineering research. Until the mid-1900s, researchers evaluated the site and structural response independently. With the advancements of soil dynamics, we have learned that stiff foundations embedded in a softer domain filter the incident waves, and the compliance between soil and foundation allow the rocking of superstructures. These interactions increase the damping of the system and thus decrease the loading and deformation of buildings (Sarrazin 1970; Sarazzin et al. 1972; Aspel and Luco 1987; Housner 1957). These observations led engineers to implement soil–structure interaction (SSI) into seismic design.

SSI is the interaction between a stand-alone building and the flexible soil which it is resting on. Neighboring structures are not considered. On the other hand, site–city Interaction (SCI) is the interaction between neighboring buildings through the connecting medium, i.e. soils. The key phenomena of SCI and SSI are shown in Fig. 1. Despite the advancements in SSI, without the concept of SCI, engineers remained unable to explain some unexpected performance of buildings and erratic damage patterns observed after major earthquakes, such as events in Mexico, Italy, and Japan (Uenishi 2013, 2010; Guéguen et al. 2002). In the 1985 Mexico City earthquake, elongated duration, and monochromatic beatings (viz. Fig. 1a) were identified in the earthquake records. Bard et al. (1996) explained these phenomena as ground motion contamination by the multiple interactions between the soil and closely-spaced structures. Considering the collective dynamic behavior of a group of buildings, Uenishi (2010, 2013) explained why neighboring buildings with almost identical dynamic properties would experience vastly different damage levels during the 1976 Friuli earthquake in Italy and the 2007 Noto Peninsula earthquake in Japan.

With cities ever-expanding, a key pursuit of earthquake engineers is a more rigorous hazard prediction to ensure safe urban planning and resilient seismic design. Understanding site–city interaction (SCI) is an essential part of this pursuit. SCI can be described
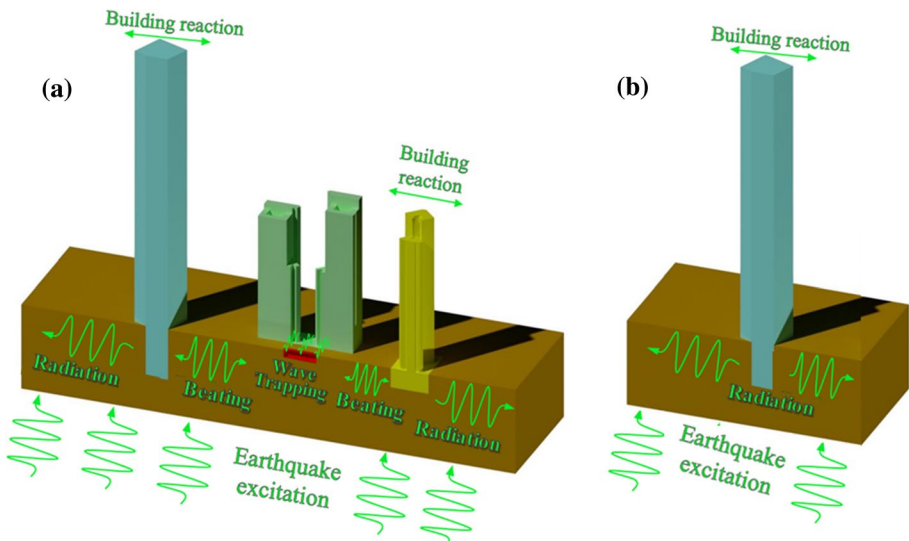

Fig. 1 Key phenomena of the **a** site–city interaction and the **b** soil–structure interaction models used in this study

as the cumulative effect of site response and both underground, and above ground structure to structure interaction via the soil. Figure 1a shows some of the key phenomena of site–city interaction. Beating encompasses the vibrations fed back to the soil from the seismic response of buildings and the disturbance of ground motion created by the reflected/refracted waves at soil–foundation interfaces. These waves can either radiate or interact with neighboring buildings. During an earthquake, super-tall buildings can pin their surrounding soil mass in place via their foundation due to their immense weight. Furthermore, closely-spaced underground structures can trap surface waves in the soil between them. Active SCI effects include inertial effects and feedback vibrations from the buildings' seismic response (Guéguen and Bard 2005). On the other hand, passive SCI effects include wave reflections and refractions at soil–foundation interfaces generated due to impedance contrasts and the pinning effect of foundations (Kato and Wang 2019; Semblat et al. 2008). As shown in 2D and 3D general parametric studies (Luco and Contesse 1973; Kham et al. 2006; Bard et al. 2006), these SCI effects might manifest in energy exchange between buildings via the soil or in resultant waves traveling outward from a cluster of buildings, thus, increasing the seismic demand in neighboring areas. Consequently, a structure can be considered as the source of a secondary wavefield that contaminates the ground motion and affects neighboring buildings (Lin et al. 1987; Mason et al. 2013; Isbiliroglu et al. 2015; Schwan et al. 2016). It is important to mention that soil layering is key in SCI, as surface waves are strongly affected by soil heterogeneity. Many of the described SCI effects are governed by the interactions of these waves. Through a 2D parametric study, Guéguen et al. (2002) in their study of an idealized city over a basin showed that ground motion contamination due to SCI is not a local, but a regional-scale, more precisely, a basin-scale phenomenon. Hence, in populated cities regional-scale simulations considering all structures would result in a better seismic hazard prediction. Moreover, the effects of SCI become increasingly important for urban infrastructure developed over long periods. In urban expansion projects, new buildings, underground stations, or subways are often constructed in multiple phases in the vicinity of existing buildings. Disregarding SCI effects from the modified configuration on the pre-existing structures can jeopardize their seismic resilience. To this end, the conventional seismic design of a standalone structure is not comprehensive and potentially unsafe. This was expressed by several general purpose SCI studies, such as Semblat et al. (2008) and Tsinidis (2018).

Although significant progress has been made on the topic of SCI, some aspects remain unclear. Urban districts tend to have heterogeneous or special building layouts containing structures with diverse shapes and sizes. Furthermore, due to the vertical expansion in metropolitan environments, super-tall buildings with deep foundations and large underground chambers are often simultaneously present. Several research groups have suggested the relevance of these structures and their 3D distribution to SCI (Semblat et al. 2008; Bard et al. 2006; Chen and Li 2015; Verona et al. 2021). However, the combined effects of underground and aboveground structures have not been investigated before. Realistic 3D layouts such as buildings surrounding a center plaza and the SCI of super-tall buildings have not been considered either. SCI effects inside a city have been deemed potentially beneficial or harmful, depending on the building configuration, site conditions and input motions. Within a dense building cluster, SCI generally reduces the site and structural responses under the double resonance condition, i.e. when the fundamental frequencies of the site and buildings are close to each other and they resonate under excitation. This has been confirmed in a couple of parametric studies on idealized cities laying over basins (Sahar et al. 2015; Semblat et al. 2008). However, multiple factors can change the beneficial effect of SCI into an adverse effect. Some important factors, such as the lack of double resonance,

the heterogeneity of building types, their irregular distribution, and their spacing, can contribute to the development of adverse SCI effects. These factors are complicated and their simultaneous contributions are difficult to quantify, hence, an exact delineation has not been made between beneficial and adverse SCI. It is noteworthy, however, that in all cases SCI generates an outward propagating wavefield from a city that increases demand in the outskirts (Semblat et al. 2008; Bard et al. 2006). According to case studies on dense urban sites (Kato and Wang 2021; Taborda and Bielak 2011), in the vicinity of tall building cluster, the SCI effects may increase high-frequency components of motions due to wave trapping, therefore, increase the seismic demand on neighboring short-story buildings.

This case study examines SCI effects under a more realistic scenario that might provide better insight. The contribution of SCI to structural response must be isolated from SSI then quantified to improve our understanding of the phenomenon. Hence, this study aims to capture and quantify the complex interaction that occurs between underground structures and super-tall buildings in a 3D setting. We carry out a site–city interaction case study in Hong Kong based on Kowloon Station and its surrounding structures to bridge the aforementioned knowledge gaps. A fully integrated 3D model of the Kowloon transportation hub was built for a numerical analysis. The model includes 16 high-rise buildings distributed in a trapezoidal layout. The buildings surround a center plaza with a metro station underground. A discontinuous Galerkin spectral element code (Mazzieri et al. 2013) is employed to simulate 3D viscoelastic wave propagation in the studied models. We examine the influence of super-tall buildings, underground structures, and a special building layout on both structural and site responses. Besides the fully integrated SCI model of the entire building cluster (hereinafter referred to as the "SCI model"), we build standalone models (as shown in Fig. 1b, hereinafter referred to as the "SSI model") of four chosen buildings in the development. The standalone models are created in the same fashion as the SCI model (i.e., the soil and the structure are modelled using solid hex elements) except that they only contain a single building without its neighbors (viz. Fig. 1b). Through comparing these models, we isolate and quantify the effects of SCI on structural responses. In the end, we discuss the key phenomena of SCI and their engineering implications on seismic resilience at congested urban sites.

2 Simulation setup

2.1 Computational platform

The most popular methods used to simulate large-scale wave propagation are the boundary element (BEM), finite difference (FDM), finite element (FEM), and spectral element methods (SEM). All these methods can be used for large-scale seismic simulation. There are several grand challenges in simulating regional-scale events in three-dimensions. Site–city interaction models have an immense number of DOFs, hence the effectiveness and efficiency of the numerical solver are crucial. The complexity of structural shapes and the multi-scale nature of a city model makes meshing a challenging task.

In this study, we use the numerical code SPEED (Mazzieri et al. 2013; Paolucci et al. 2015; Infantino et al. 2020). This code implements a discontinuous Galerkin formulation of the spectral element method (DGSEM). We chose the DGSEM as it eases some of the meshing challenges faced in large-scale SCI simulations as we will discuss in the following sections. SEM, in principle, is a high order FEM (h–p implementation)

that uses high order piecewise polynomials as its basis function. In SEM, the colloca-
tion points are chosen to be the $N+1$ Legendre–Gauss–Lobatto (LGL) points which
are the roots of $(1-\xi^2)L_N{}'$, where $L_N{}'$ is the derivative of the Legendre polynomial of
degree N. This choice is motivated by the fact that Lagrange polynomials defined on
these collocation points for interpolation, combined with the use of the LGL quadrature
on the same points leads to an exact diagonal mass matrix. Moreover, with this imple-
mentation the equations of motion are satisfied at all internal LGL nodes. Therefore,
SEM has been increasingly used in large-scale wave simulation in recent years (Chaljub
et al. 2010; He et al. 2015; Wang et al. 2018; Lu et al. 2018; Huang et al. 2020, 2021;
Feng et al. 2022). Figure 2a shows 3D illustration of the LGL points along with the
Lagrange basis functions on an SEM element. Interpolation in the elements are done via
the Lagrange interpolation scheme. Here the governing equation of motion is according
to Eq. (1).

$$\rho\boldsymbol{u_{tt}} + 2\rho\xi\boldsymbol{u}_t + \rho\xi^2\boldsymbol{u} - \nabla\boldsymbol{\sigma}(\boldsymbol{u}) = \boldsymbol{f} \tag{1}$$

where $\boldsymbol{u}_t$ and $\boldsymbol{u}_{tt}$ are the first and second temporal derivate of displacement, $\boldsymbol{u}$, respectively.
$\boldsymbol{f}$ is the body force, $\boldsymbol{\sigma}(\boldsymbol{u})$ is the Cauchy stress tensor, ρ is material density. Note that in Eq.
(1), two equivalent body forces, $2\rho\xi\boldsymbol{u}_t + \rho\xi^2\boldsymbol{u}$, are introduced to model anelastic attenua-
tion by multiplying the velocity and displacement field with a decay factor ξ. The strategy
is similar to the method proposed by Graves (1996). ξ is the decay factor equivalent to the
quality factor Q, $\xi = (2Q)^{-1}$. All frequencies are equally attenuated, leading to a frequency-
proportional quality factor, $Q = Q_0$ (f/f_0), where Q_0 is the quality factor evaluated at a refer-
ence frequency, f_0.

A diagonal mass matrix combined with an explicit time marching scheme is very
important for parallel implementation, and thus for the efficiency of solving large-scale
wave propagation problems. The DGSEM software used in this study adopts the stand-
ard leapfrog scheme for time marching using the following algorithm: the nodal velocity
vector is defined as $\mathbf{V} = \dot{\mathbf{U}}$ and the initial conditions are set to $\mathbf{V}(t_0)$ and $\mathbf{U}(t_0)$. The simu-
lation time $[0, T]$ is subdivided into k time steps $t_n = \Delta t, 2\Delta t, …, k\Delta t$, where $\Delta t = T/k$.
Then the explicit 2nd order leap frog scheme corresponds to:
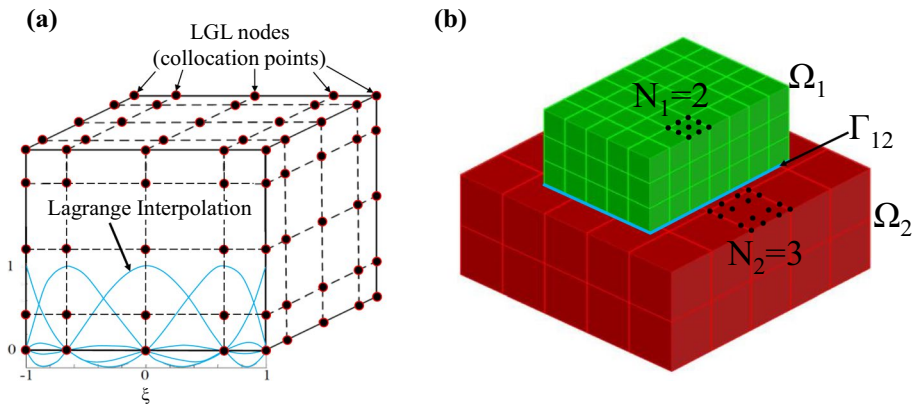

Fig. 2 **a** $N=4$ SEM element showing the LGL points along with the Lagrange basis functions. **b** The visu-
alization of a simple non-conforming mesh consisting of two subdomains, Ω_1 and Ω_2, with a discontinuous
interface Γ_{12} between them

$$\mathbf{M}(t_{n+1}) = [2\mathbf{M} - \Delta t^2 \mathbf{K}]\mathbf{U}(t_n) - \mathbf{M}\mathbf{U}(t_{n-1}) + \Delta t^2\ \mathbf{F}(t_n) \tag{2}$$

for $n = 1, \ldots, k$, with

$$\mathbf{M}(t_1) = \left[\mathbf{M} - \frac{\Delta t^2}{2}\mathbf{K}\right]\mathbf{U}(t_0) - \Delta t\mathbf{M}\mathbf{V}(t_0) + \frac{\Delta t^2}{2}\mathbf{F}(t_0) \tag{3}$$

where $\mathbf{M}$ is the mass matrix, $\mathbf{K}$ is the stiffness matrix, and $\mathbf{F}$ is the vector of externally applied loads including the absorbing boundary conditions. This scheme will only remain stable if the size of Δt satisfies the Courant–Friedrichs–Levy (CFL) condition, $\Delta t \leq CCFL \cdot \Delta x / V_p$, where V_p is the compressional wave velocity, Δx is the shortest distance between two LGL nodes, and CCFL is a constant that can be approximated as CCFL $\approx N-$ 2. According to error estimate analysis conducted by Antonietti et al. (2012), this scheme coupled with the DG formulation will provide sufficient accuracy provided that there are 5 LGL points per minimum propagated wavelength.

The discontinuous Galerkin (DG) formulation of SEM provides an easy discretization of complex domains and mesh adaptivity, by allowing for neighboring subdomains with non-matching interpolation order (N) and mesh size (h). The mesh can abruptly change between non-conforming volumes, and each non-conforming volume can be meshed independently, which allows for a significantly easier meshing procedure and higher quality mesh. This way, the number of unknowns in a geometrically complex problem, and thus the computational cost of the analysis can be greatly reduced (Paolucci et al. 2014). A visualization of a simple non-conforming mesh is shown in Fig. 2b. The continuity of the global solution over non-conforming interfaces is imposed inherently in the DG formulation by the symmetric interior penalty Galerkin method (Rivière 2008). The jump of stress and displacement are quantified and penalized across discontinuous interfaces (Antonietti et al. 2012). However, numerical instabilities may occur hence the penalty parameters should be chosen carefully.

2.2 Computational models

The testbed for this study (Fig. 3), the Kowloon metro station, is one of the busiest and most populated transportation hubs in Hong Kong. The 12 m deep metro station supports an additional 18-m superstructure, which is surrounded by 16 super-tall buildings, including the 480 m tall International Commerce Centre, the tallest skyscraper of Hong Kong. This testbed is ideal for examining the interactions between underground structures and building layout effects on SCI. Furthermore, Kowloon station is a densely populated site representing high economic value, and it is subjected to further development. The

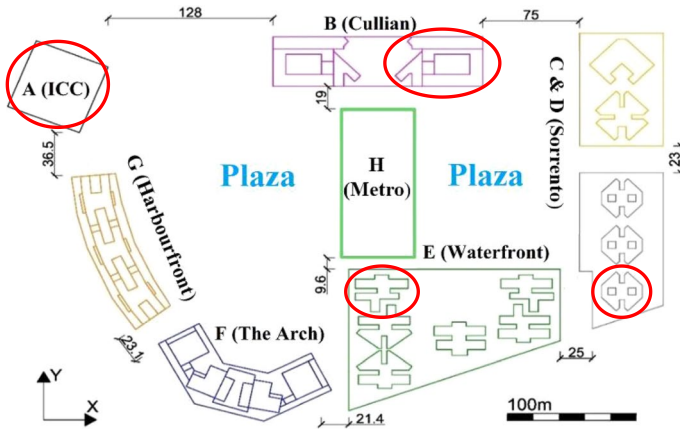**Fig. 3** Testbed for this study—Kowloon station, Hong Kong

Fig. 4 2D layout of Kowloon station. Red circles indicate the structures chosen for SSI–SCI comparison

arrangement of the structures, as shown in Fig. 4, is typical of transport hubs in Hong Kong and many major cities of the world. We examine ground motion contamination through the fully integrated SCI model of the entire study area. The variation in height, complexity, and foundation depth of the structural systems are large, resulting in significant inertial differences between the two sides of the hub, i.e., between the area around structures **A**, **B**, **F**, **G**, and **C**, **D**, **E**, according to Fig. 4. Besides the SCI model, we created four SSI models based on building clusters **A**, **B**, **D**, and **E**. Superstructures in clusters **B**, **D**, and **E** stand on a single raft foundation supported by piles. Hence, we consider the entire cluster in a single SSI model for these clusters to honor their design. From each cluster, we chose a single superstructure, indicated by red circles in Fig. 4, to compare SSI and SCI models. The geometric and geological properties of the models are based on architectural, geotechnical, and geological data acquired from the Hong Kong Buildings Department (HKBD) (Hong Kong Buildings Department 2019). Dynamic parameters of the soil layers and the structures are derived from these data and are described in the following two sections. The simulation domain is $5.4 \times 5.4 \times 0.15$ km in size, while the area of the development is 1.4 km^2. Data derived from the synthetic recordings on a dense monitoring grid are subsequently animated and highlighted in cartoons.

2.3 Soil model and parameters

Soil conditions at the site are typical of Hong Kong's harbor front. Based on borehole data acquired from the HKBD, three geological layers were identified: hydraulic fill, completely decomposed granite (CDG), and fresh granite. We built a five-layer model, shown in Fig. 5b, following the *SPT-N* data described in Table 1. We defined a piecewise linear shear wave velocity profile using *SPT-N-V$_s$* correlations published by Wair et al. (2012) that accounts for overburden pressure. The simulations use a Poisson's ratio of 0.33 ($V_p = 2V_s$), which is typical for elastic soils and ensures the stability of the bottom absorbing boundary (Stacey 1988). Boundary nodes were fixed in 'y' and 'z' on the edges of the domain, but free in 'x' direction to mimic a shear box. In addition, the computational domain is extended by 5 times of the size of the building cluster in each direction. The domain is 5.5 km in 'x' and 'y' directions, while the dimensions of the building cluster is 500 m by 300 m. Surface waves generated at
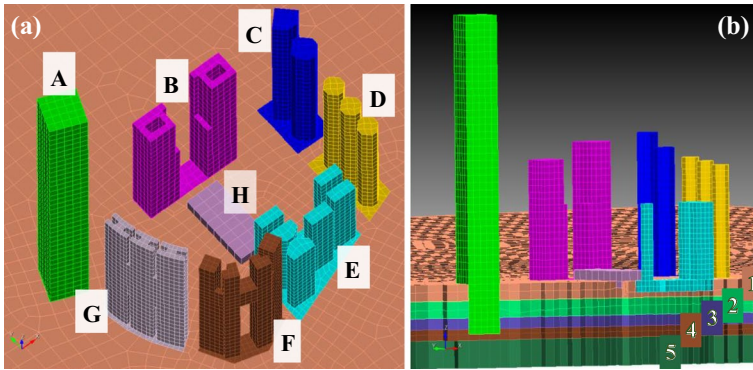
Fig. 5 Non-conforming subdomains (**a**), soil layers (**b**) and meshed geometry for the SCI model

the building cluster dissipate due to material and geometric damping in the extended domain. There are no significant wave reflections from the boundary. The controlling earthquakes in Hong Kong are a magnitude $M_w = 6$, rupture distance $R = 30\,km$ event in the short period range of the uniform hazard spectrum (UHS), an $M_w = 7$, $R = 60\,km$ event for a spectral period of around 1 s, and an $M_w = 7.75$, $R = 300\,km$ event for long period range (5 s). The design ground motion library (Wang et al. 2015) was used to select a time history that can be fitted to the 2475-year return period UHS prescribed by Hong Kong's design practice (ARUP
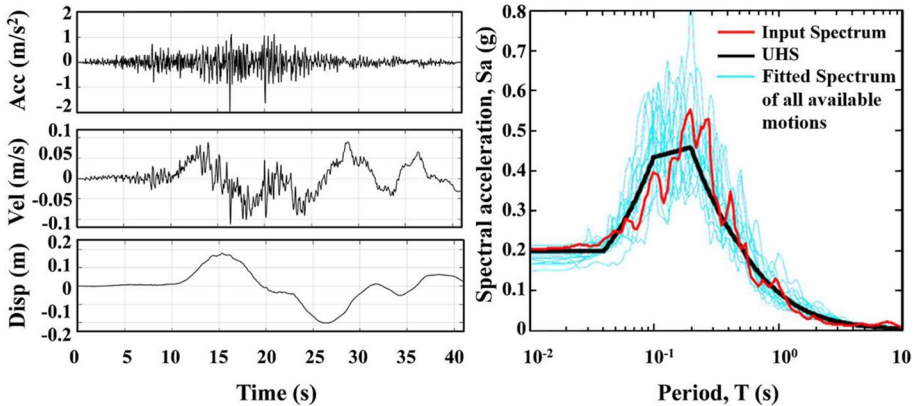

Fig. 6 The input signal (as rock outcrop motion) and its acceleration spectra compared to the 2475-year return period UHS for Hong Kong

Table 1 Soil properties

ID	Soil type	Layer thickness (m)	SPT-N	V_s (m/s)	ρ (g/cm^3)	Q_0
1	Fill	30	28	230	2.0	10
2	CDG	30	50	400	2.0	30
3	CDG	20	70	450	2.0	30
4	CDG	20	80	480	2.0	30
5	Granite	50	>200	2000	2.6	100

2015). The selected signal (see Fig. 6) was then truncated and baseline corrected, and finally deconvoluted to the bedrock. The '*x*' component of this motion was applied at the bottom of the simulation domain as a vertically propagated shear wave input, which is usually assumed for design purposes. Furthermore, only the '*x*' direction input is used in order to highlight the SCI effects. The fundamental period of the site is 0.91 s, while the predominant period of the excitation is 0.45 s. Although a site resonance is not expected, the period gap is small enough to cause significant ground motion amplification. The majority of the excitation energy is contained between 1 and 7 Hz, hence, $f_0 = 4$ Hz was adopted as the reference frequency for damping. A linear soil model may significantly overestimate the ground accelerations. To avoid this, we accounted for a strain-compatible modulus and damping ratio for each soil layer and determined the soil quality factors accordingly similarly to the equivalent linear approach (Idriss and Sun 1993; Pitilakis and Clouteau 2010). We ran a series of trial simulations to determine the averaged strain level in each soil layer, and adjusted soil modulus and damping according to the equivalent maximum shear strain ($0.65\gamma_{max}$) in each layer. We adjusted the quality factor values according to the damping curves published for hydraulic fill (Chandler and Su 2000) and CDG (Gu 2012). For the fresh rock, we assigned $Q_0 = 100$, a common quality factor for granite. Finally, the target mesh size for the unstructured meshing was set to $h = 20$ m in the topsoil layer with an $N = 3$ polynomial degree for the shape function to reach sufficient numerical accuracy, up to 6 Hz.

2.4 Structural models and parameters

Structural plans were provided by the HKBD. We model the foundation-superstructure systems as 3D homogeneous equivalent blocks. The blocks consist of the same viscoelastic hexahedral elements as the soil. This model is capable of capturing the shear, rotational, and flexural responses if the mesh is sufficiently fine, and the first derivative of the shape function is continuous between elements (C1 continuity). Such a model may be considered as the 3D generalization of the classical bending beam model. In previous 3D SCI studies, this type of model was used as a reasonable approximation of shear and bending responses of buildings (Taborda and Bielak 2011; Mazzieri et al. 2013; Isbiliroglu et al. 2015). We simplified and modeled the building geometries in CAD and selected their dynamic parameters to best represent their real behavior. The four most important parameters are shear wave velocity, V_s, mass density, ρ, fundamental period, T_0, and quality factor, Q. Taborda and Bielak (2011) suggested estimating an equivalent V_s for homogeneous block models using the empirical formula, $V_s = 28h_s$, where h_s is the inter-story height. We used the V_s values listed in Table 2. To define appropriate V_s for the smeared foundation blocks, we calculated the weighted average of the stiffness and density of soil and concrete according to their areal ratio through Eq. (4) (note $V_s^2 = G/\rho$). We calculated the average mass density for each equivalent block from the total weight and volume of each building. The total weight includes an additional 25% of the live loads. We set all superstructure densities to 300 kg/m^3 as they were all close to this value, as Table 2 indicates. We calculated the mass density of foundations following the same principle as for V_s, using Eq. (5).

$$V_s^f = \frac{A_p}{A_f}\sqrt{\frac{G_c}{\rho_c}} + \left(1 - \frac{A_p}{A_f}\right)\sqrt{\frac{G_s^{avg}}{\rho_s^{avg}}} \tag{4}$$

Table 2 Structural parameters

ID	Name	Structure	Story height (m)/soil pile ratio	Height/depth (m)	T_0 (s)	V_s (m/s)	ρ (g/cm³)	G_{avg} (Mpa)
A	ICC	Super structure	4.3	480	11.2	120	0.3	4.3
		Foundation	0.233	89	–	980	2.08	1996
B	The Cullian	Super structure	3.3	215; 244	6.5; 7.3	92	0.32	2.6
		Foundation	0.104	40	–	683	2.01	937
C	Sorrento tall towers	Super structure	3.15	243	7.7	88	0.33	2.3
		Foundation	0.065	34	–	557	1.99	617
D	Sorrento short towers	Super structure	2.95	208	7.1	83	0.33	2
		Foundation	0.065	34	–	557	1.99	617
E	Waterfront	Super structure	2.8	138	5.0	78	0.35	1.8
		Foundation	0.037	20	–	439	1.97	380
F	The Arch	Super structure	3.2	225	7.0	90	0.3	2.4
		Foundation	0.104	40	–	683	2.01	937
G	Harbourfront	Super structure	3	245	8.2	84	0.37	2.1
		Foundation	0.166	55	–	839	2.04	1437
H	Metro station	Super structure	5	30	2.5	1250	2.5	3906
		Foundation	–	–	–	–	–	–

$$\rho_f = \frac{A_p}{A_f}\rho_c + \left(1 - \frac{A_p}{A_f}\right)\rho_s^{avg} \tag{5}$$

where A_p is the total cross-section area of piles, A_f is the total foundation area, G_s^{avg} and ρ_s^{avg} are the averaged stiffness and density of soil layers encompassing the piles, ρ_c, and G_c are the density and stiffness of concrete, respectively. The natural period of buildings can be estimated based on the number of stories (N_s) they have, as $T_0 = N_s/10$. By examining Table 2, we can see that the fundamental period of all superstructures (**A–G**) is between 5 and 11 s, which falls into the long-period, low-amplitude range of the input spectrum, showed in Fig. 6. Based on this observation, the buildings are expected to experience low-to-moderate roof displacement, as this is mainly governed by the resonance response. Finally, based on structural design practice in Hong Kong, we used a quality factor Q_0 = 100 for the superstructures, while $Q_0 = 200$ was assigned for the foundations based on their stiffness. We modeled the metro station and its superstructure as a closed rigid box, which has dimensions $57 \times 127 \times 30$ m and is buried 12 m into the soil. We assigned concrete material properties to the box that gives it significant weight and stiffness.

The DGSEM makes meshing easier as the domain can be discretized into non-conforming sub-domains. We created nine sub-domains for each building cluster and the soil, which we meshed independently, then assigned discontinuous interfaces between the soil and each foundation. Consequently, the resulting mesh has very high-quality metrics. Figure 5a shows a visualization of the subdomains and the mesh. Each color in Fig. 5a represents a non-conforming sub-domain. Superstructures and foundations have a mesh size ranging from 8 to 15 m. Capturing the flexural mode of high-rise buildings is important, thus, we specified the mesh size such that the models can effectively capture the bending moments of the buildings. The narrowest cross sections of a building consist of at least two 2nd order elements (i.e. 6 interpolation points) in each direction. The mesh is fine enough to capture the bending moment within the structure reasonably well. The superstructure models are accurate at least up to 5 Hz. Subsequently, we created the four standalone SSI models of **A**, **B**, **D**, and **E** in the same fashion. We note that the SCI model contains 117,163 elements, and it costs 2150 core hours to run the 42-second scenario with a 0.0001 s time-step on our server with 2.9 GHz Xeon CPUs and 190 GBs of RAM.

3 Results

3.1 SCI Effects on site response

In this section, we will discuss how structures contaminate ground motion through their interaction with each other via the soil. Figure 7a shows a snapshot of the 'x' component wavefield at the moment of peak ground displacement (PGD). The peak ground perturbation (PGP) field relative to the free-field displacements (cf. Eq. 6) is shown in Fig. 7b.

$$u_p(t, x_i) = u(t, x_i) - u(t, x_{ff}) \tag{6}$$

where $u_p(t,x_i)$ is the displacement perturbation at monitor point x_i, $u(t,x_i)$ is the displacement at x_i and $u(t,x_{ff})$ is the displacement at the free field.

The wavefields show a clear disturbance in the ground motion due to the presence of buildings. Figure 7a shows displacements reaching the PGD (20 cm) in several regions,
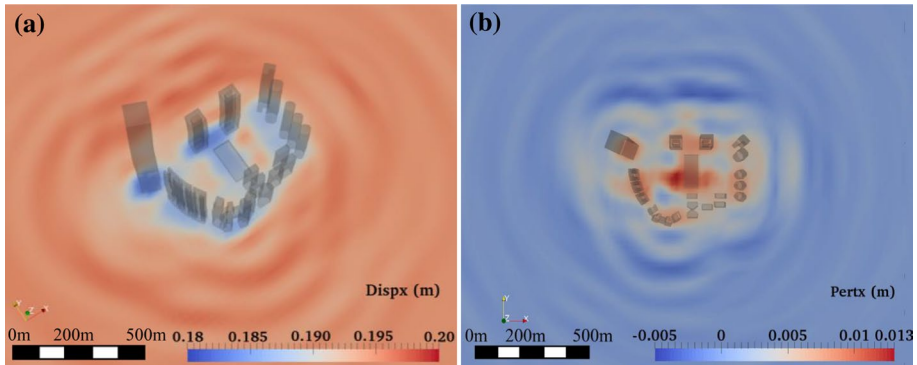
Fig. 7 Site response at the instance when PGD **(a)** and PGP **(b)** occur

including on both sides of the metro station in the center plaza and in the outskirts of the development, up to 300 m away from the structures. Two phenomena of SCI can be recognized in Fig. 7b that are influenced by the building distribution. First, an outward propagating wavefield is visible assuming the shape of the building layout. Second, significant perturbations, that we describe as wave trapping, occur in the center plaza amid structures. The outward propagating wavefield has been identified in 2D studies before (Bard et al. 2006). However, our results show that the 3D building distribution can have a profound effect on the propagation path of these waves. Due to their high inertia, super-tall buildings pin their neighboring soil mass via their stiff foundations. This is the primary cause of the perturbations in the outskirts. The literature regards this as the passive effect of structures in SCI, where buildings act as obstacles for the propagating wave. On the other hand, the trapped wavefield is caused by the presence of underground structures. Surface waves may get trapped in the soil enclosed by underground structures. As the major energy dissipation happens through radiation damping, waves trapped in a small area may reflect at soil–foundation interfaces multiple times. This can lead to constructive interference and significant ground motion amplification.

Figure 8a shows the 'x' component peak ground accelerations (PGA). In the close vicinity of the foundations and the center plaza, the PGA is over 6 m/s^2. Specifically, around points **1**, **3**, and **4** indicated in Fig. 8b, the PGA reaches 6.5 m/s^2. In addition to the large 'x' PGA, the interaction between structures and the soil generates considerable 'y' and 'z' (vertical) acceleration components as well, shown in Fig. 8c, d, respectively. The rocking of the buildings causes at least 1.5 m/s^2 'z' acceleration in the center plaza and up to 100 m on either side of the development. While misaligned wave reflections from the obliquely oriented foundations generate 'y' accelerations up to 4 m/s^2 in the center plaza. Figure 8b shows the PGA amplification map. Amplification factors range from 1.1 to 1.65 in the center plaza, which shows that wave trapping can dramatically increase the surface response when it occurs. In the outskirts (points **5–8**), alternating ring-like zones of amplification/no-amplification emerge. Waves reflected from foundation-soil interfaces that travel outwards interfere constructively/deconstructively with incoming shear waves. The alternation patterns are associated with wavelengths varying from 30 to 100 m, corresponding to a period range of 0.1–0.4 s. As longer period waves can travel farther, amplification zones far from the structures recur about every 100 m, while close to the structure the recurrence length is about 30 m. The outward propagating wavefield travels up to 300 m,
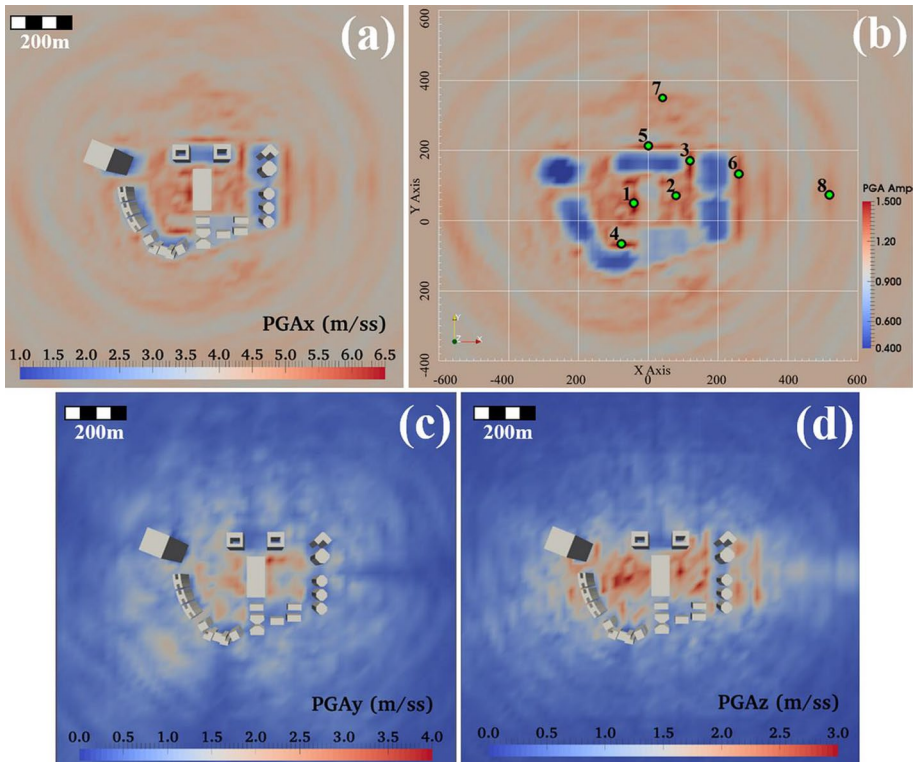
Fig. 8 PGA maps in '*x*' (**a**), '*y*' (**c**), '*z*' (**d**) and PGA amplification map showing the monitoring points used for spectral analysis (**b**)

where an amplification factor of 1.1–1.2 persists. The 20% excess acceleration $(0.7 \, \text{m/s}^2)$ is larger than the PGA of a serviceability level earthquake (SLE) specified by the Chinese seismic design code.

The pseudo acceleration spectra (*Sa*) in Fig. 9 shows a significant amplification of the free-field (FF) motion in the short period range (up to 0.3 s) at the center plaza and close to the foundations (points **1**–**6**). However, as we move away (points **7**, **8**), the spectral amplifications diminish. It is also interesting to notice that the spectral ordinate considerably increases at 0.4 s moving far from the structures (point **7**, **8** vs. **5**, **6**). These observations are consistent with our argument above regarding the ring-like PGA amplification patterns. On the other hand, Fig. 9 shows no change in *Sa* in the period range of 1–10 s, where the site or building resonance would occur. Active beating of structures would trigger amplification in the ground motion around the natural period of the local structures which cannot be identified. From this, we can conclude that ground motion amplification results solely from wave trapping between the underground structures, from the pinning effect of foundations, and by structures acting as obstacles to propagating seismic waves. These phenomena seem to dominate in the short period range in the presence of super-tall buildings. The level of amplification observed due to SCI raises concerns for the possible increase in seismic demand on secondary structures in the neighborhood of super-tall buildings, for example, footbridges, low-rise buildings up to 3 stories, and temporary structures such as market boutiques or stages for large social events.
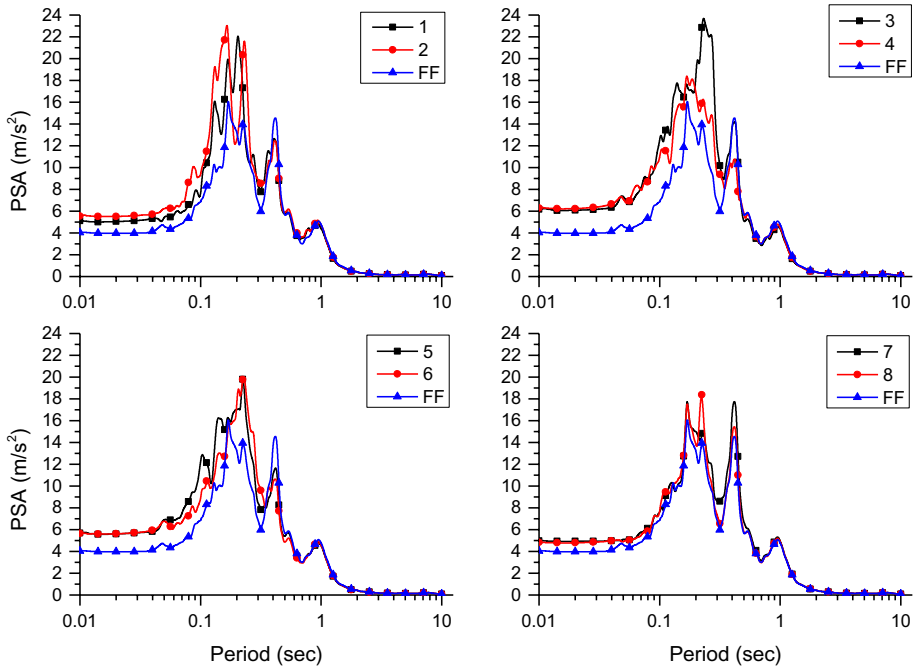
Fig. 9 Comparison of pseudo spectral acceleration at free-field (FF) and points 1–8

In the following, we discuss ground velocity signal energy, defined in Eq. (7):

$$E = \int_{t0}^{T} v(x,t)^2 dt \qquad (7)$$

where E is the velocity signal energy and $v(x, t)$ is the velocity signal at monitor point x integrated from the initial time (t_0) until the end (T) of the signal. The velocity signal energy differs from the definition of cumulative kinetic energy density only by a scalar term. Therefore, it is indicative of the intensity of ground motions.

Figure 10 shows the map of velocity signal energy ratios (ER) between the SCI and the free-field response. Compared with the PGA amplification map in Fig. 8, the ER map shows a similar but more distinct pattern. Reduced ER zones are observed around the building foundations. This displays how structures act as energy barriers and energy sinks via their foundations. Foundations decrease energy by 40–60%. High energy reduction is associated with large building inertia, and with a stronger pinning effect of deeper foundations. On the left and top side of the development, clusters **A**, **B**, **F**, and **G**, which have the deepest foundations and heaviest structures reduce ER the most. Conversely, cluster **E** reduces the energy the least, as it consists of structures with the lowest inertia and the shallowest foundation

The metro station (**H**) is relatively compliant with soil displacements and only causes slight energy reduction. However, it takes a crucial role in the interaction between underground structures by acting as an obstacle for incoming and trapped waves. The ER map shows focused zones of increased energy (110–130%) due to wave trapping on both sides of the metro station. From the acceleration spectra at points **1** and **2** in Fig. 9, we can see
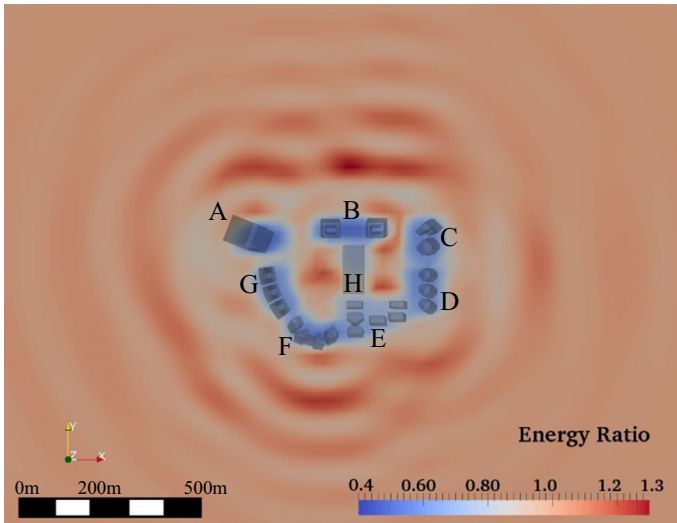
Fig. 10 ER, velocity signal energy ratio map

that only short periods are amplified. However, we speculate that as the entrapment zone gets larger and longer waves can be trapped as well, amplification would occur at longer periods.

To demonstrate the importance of the structure layout on the wave trapping effect, the metro station (H) in the central plaza is removed as an alternative urban scenario. Figure 11 compares the ER and PGA maps with and without the metro station, using a 2 Hz
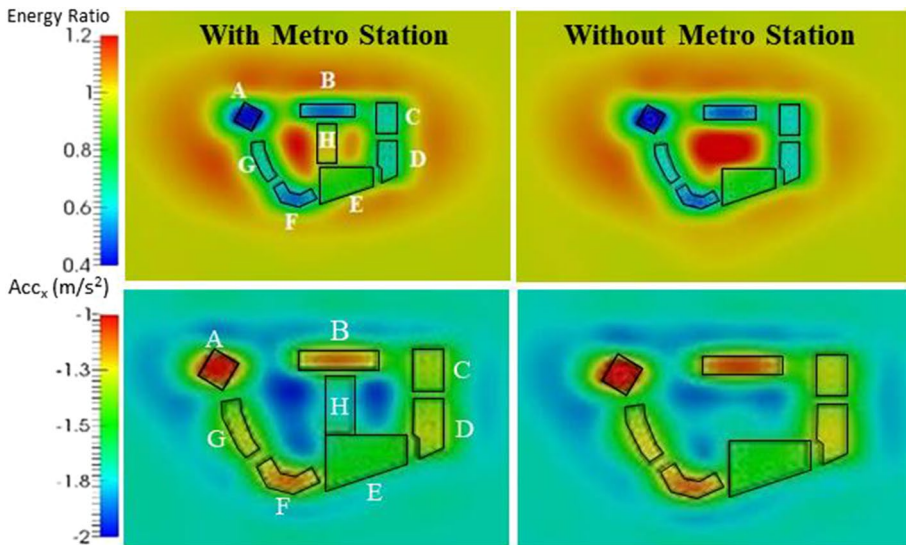

Fig. 11 Signal energy ratios between SCI and freefield energy (top) and peak ground accelerations (bottom) with and without the presence of the metro station (H)

Ricker wavelet as the input motion for easier comparison. It shows that if the metro station is absent, the center plaza has a larger and more homogeneous zone of ER amplification. On the other hand, the metro station spatially divides the plaza into smaller unbuilt zones, which traps higher frequency waves, and thus the PGA is increased in these divided zones when the metro station is present. Finally, we emphasize that despite the small ratio between the fundamental site period and the fundamental period of buildings, the immense inertia of super-tall buildings and wave trapping will still cause notable SCI effects.

3.2 SCI effects on structural response

In this section, we quantify the contribution of SCI to the structural response of clusters **A**, **B**, **D**, and **E**. Figure 12a, b shows snapshots of building and soil deformations when the roof displacement of structures **E** reaches negative and positive peak values, respectively (at times: 31 and 40 s). The equivalent homogeneous block structure models can capture flexural and modal responses as expected from a 3D beam. This is well demonstrated in Fig. 12 for structures **A** and **E**. Structures in **E** are dominated by their first modal response, however, perturbed with high-frequency modal shapes. Other structures respond more significantly in higher modes and torsional modes due to their misalignment with the '*x*' directional excitation and their non-trivial geometry. Figure 12 also shows that the base of the buildings and their surrounding soil do no move together. This phenomenon contributes to the beating effect. However, active beating is not visible in our case, as the spectrum (*Sa*) at the natural period of the structures is negligible (cf. Fig. 9) and the high-frequency vibrations of buildings contain too little energy to notably affect ground motions. The metro station is compliant with soil displacements. On the other hand, its movement is limited by its surrounding structures that stiffen the local site response.

Subsequent figures describe some quantities commonly used to describe dynamic structural response, namely, the maximum relative story displacement (MRSD), the maximum inter-story drift ratio (MIDR), and the maximum relative story acceleration (MSA) defined in Eqs. (8)–(10).
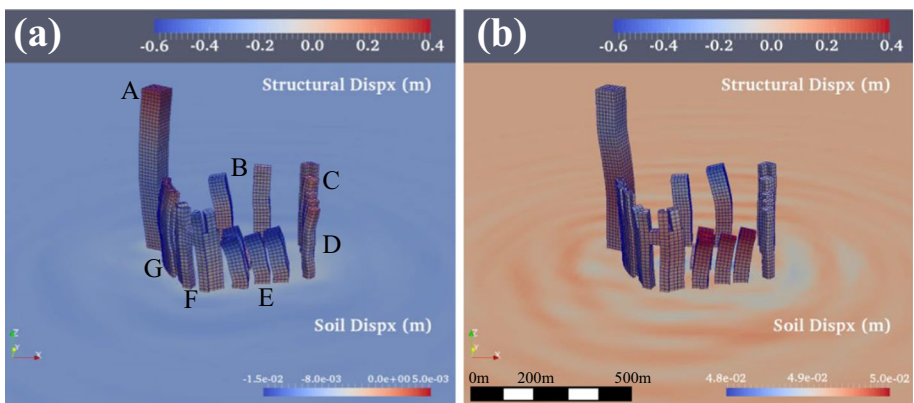

Fig. 12 Structural response of the SCI model when peak negative **(a)** and positive **(b)** displacements occur in structures E

$$MRSD_i = \max\left(u_i(t) - u_b(t)\right) \tag{8}$$

where $MRSD_i$ is the maximum relative story displacement at story i while, $u_i(t)$ and $u_b(t)$ are displacements at floor i at times t and the base of the building, respectively.

$$MIDR_i = max\left(\frac{dx_i(t)}{dz}\right) \tag{9}$$

where $MIDR_i$ is the maximum inter-story drift ratio at story i, $dx_i(t)$ is the relative horizontal displacement of the story i at times t, and dz is the inter-story height.

$$MSA_i = max\left(a_i(t) - a_b(t)\right) \tag{10}$$

where MSA_i is the maximum relative story acceleration at story i while, $a_i(t)$ and $a_b(t)$ are accelerations at floor i and the base of the building at times t, respectively.

Figures 13 and 14 compare these quantities between SSI and SCI models of the structures highlighted in Fig. 3, in clusters **A**, **B**, **D**, and **E**. Note that the resolution of the figures is according to the density of monitoring points (1 per element) and do not represent the spatial resolution of the SEM model itself (3 GLL nodes per element). The maximum relative roof displacements are between 40 and 60 cm. These values are virtually identical between SCI and SSI models. The shortest tower (**E**) shows a dominant first modal response in '*x*'
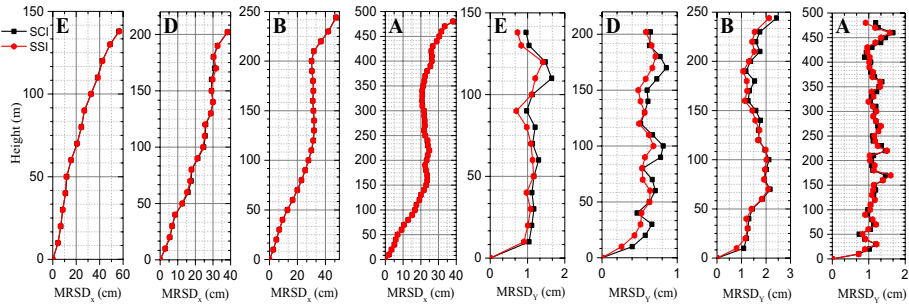

Fig. 13 Comparison of SSI and SCI maximum relative story displacements in '*x*' and '*y*' direction for structure E, D, B, and A
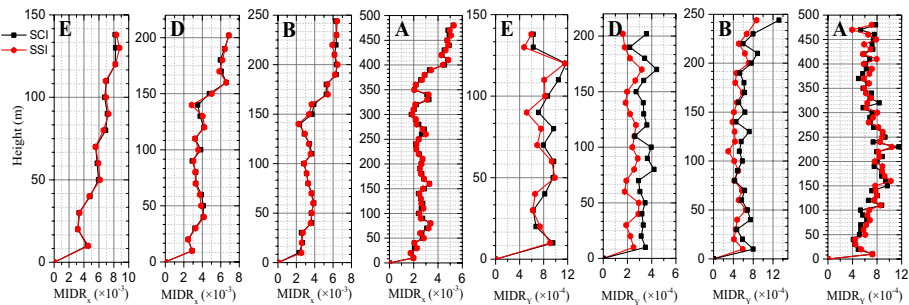

Fig. 14 Comparison of SSI and SCI maximum inter-story drift ratios in '*x*' and '*y*' direction for structure E, D, B, and A

based on $MRSD_x$ in Fig. 13. However, $MIDR_x$ in Fig. 14 reveals that the drift pattern of the building is of a higher mode. For high-rise buildings, higher-mode participation becomes important. Structure **D** primarily shows the first and second modal shapes while the first three modes dominate in **B** and **A**, according to $MRSD_x$. A substantial change in structural response between the SSI and SCI cases is not expected. Based on Fig. 9, SCI affects the short periods (0.01–0.3 s), which is far from the buildings' fundamental periods (5–11 s) and their dominant higher modes. Short period waves cannot change the displacement and deformation reaction of such tall buildings, as $MRSD_x$ and $MIDR_x$ graphs would indicate. On the other hand, upon inspecting $MRSD_y$ and $MIDR_y$ that are orthogonal to the shaking direction, a slight increase is evident for the SCI model. The increased distortion in 'y' is related to excess acceleration and large spatial incoherency of ground motions generated by SCI. It is noted that SSI models also displace in the 'y' direction due to special building geometries and misalignment with respect to the shaking direction. In conclusion, although the site response is adversely affected by SCI, super-tall buildings do not suffer significantly increased seismic demand in terms of MRSD and MIDR.

Figure 15 shows peak roof accelerations ranging from 4 to 12 m/s^2 with the largest value belonging to building **E** and the smallest to **B**. The evolution of MSA displays the most prominent differences between SSI and SCI models. Maximum relative story accelerations measured along the buildings demonstrate the notably adverse effects of SCI, in both 'x' and 'y' directions. Each building has several floors that suffer around 1 m/s^2 additional acceleration in the 'x' direction. A few floors show up to 30–40% increased MSA. Generally, MSA_y is increased on each floor by 50–100% (1–2 m/s^2) for structures **E**, **D**, and **B**, however on average only 25% (0.5 m/s^2) for **A**. The implications of increased MSA are mostly on the serviceability of buildings, possible damage to non-structural components, and building content loss.

In the following, we calculate the destructive kinetic energy injected into each building during excitation using Eqs. (11) and (12). Only velocity relative to the velocity at the base of a structure can be considered destructive, as translational motion will not increase the
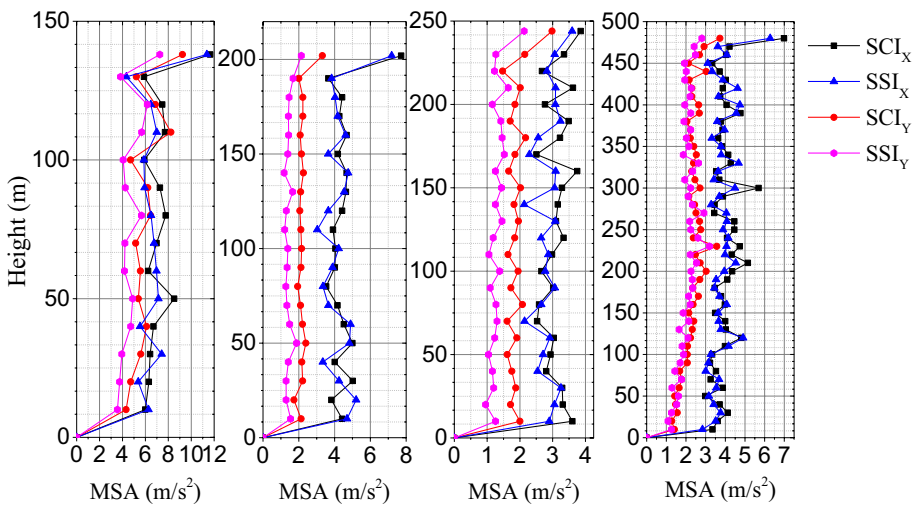

Fig. 15 Comparison of SSI and SCI maximum story accelerations in 'x' and 'y' direction for structure E, D, B, and A

demand on structural elements. Hence, destructive kinetic energy is calculated using the relative velocity.

$$e_{kd,i}(x, y, z) = \frac{1}{2}\rho \int \left(v_i(x, y, z, t) - v_{base,i}(t)\right)^2 dt \qquad (11)$$

$$E_{kd,i} = \int e_{kd,i}(x, y, z)dV \qquad (12)$$

where ρ is the material density, $v_{base, i}(t)$ and $v_i(x, y, z, t)$ are the velocities in the i direction at time t at the building base and structural points (x, y, z), respectively. The squared difference of these velocities is integrated over the duration of the signal to get the point-wise energy density in the i direction, $e_{kd,i}$. $E_{kd,i}$ is the total destructive kinetic energy in the i direction calculated by integrating $e_{kd,i}$ over the volume, V, of the superstructure.

We take the ratio of the calculated energy between the SCI and the SSI models to quantify the effect of SCI on our four test structures. Thereby, we result in a ratio that is larger or smaller than one when the SCI effect is adverse or beneficial, respectively. Figure 16 describes the distribution of energy density ratio $EDR_x = e_{kd,x}^{SCI}/e_{kd,x}^{SSI}$ along the height of structures **E**, **D**, **B**, and **A**, based on the 'x' directional velocity. EDR_x remains below 1.2 for **E**, **D**, and **A**, but it gets as high as 1.6 for **B**. Increased energy bands recur about every 30 m in a rather consistent pattern on **E**, **D**, and **B**. These bands cover about 3–6 floors (10–20 m) where the buildings would suffer significantly increased vibration from the effect of SCI. Such increased demand might raise concerns about increased local damage potential of columns and nonstructural components. Once more, we refer to Fig. 9 to explain these patterns. Due to SCI, the acceleration spectra at points **1–6** exhibit increased spectral ordinates up to 0.3 s, which corresponds to a 30 m wavelength in the superstructures. This wavelength might be associated with a high-mode vibration that contributes to the local increase of 'x' directional energy. However, this contribution becomes insignificant when examining the total energy ratio $ER_{total} = \sum E_{kd,i}^{SCI} / \sum E_{kd,i}^{SSI}$ indicated in red in Fig. 16. SCI effects do not change the ER_{total} significantly except for
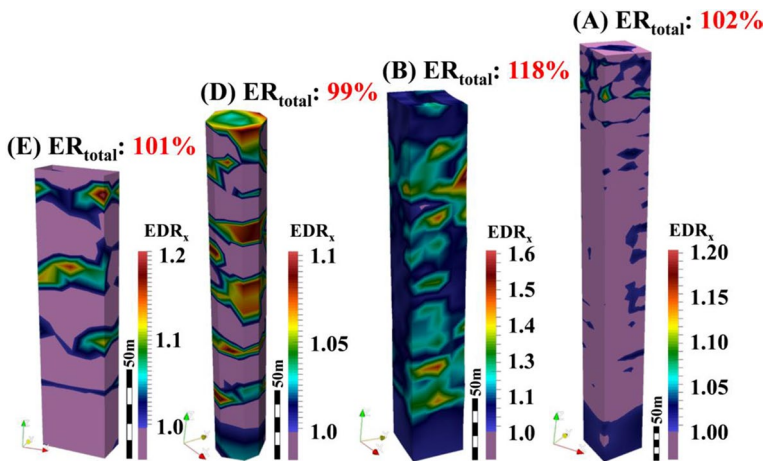

Fig. 16 Distribution map of energy ratios (ER) based on 'x' directional velocity signals and total energy ratios for structure E, D, B, and A

tower **B** ($ER_{\text{total}} = 1.18$). The notable increase in ER_{total} in tower **B** is mainly due to its location. Based on Fig. 11, the open space (75 m) between **B** and **C** seems like an appropriate dimension to channelize perturbed waves generated via interactions between underground structures in the center plaza. Due to this channelization we observe that tower **B** is surrounded by a zone of high-energy amplification. On the other hand, SCI does not affect the 'x' kinetic energy contained in the overwhelming portion of the tallest building **A** (shaded light purple). The 'x' kinetic energy only increases at its base and top which results in a slight increase in its ER_{total}. Due to its height, building **A** does not respond to high-frequency perturbations thus, we cannot observe the recurring increased energy bands.

Figure 17 breaks down the total kinetic energy in three orthogonal directions and indicates the energy ratio between the SCI and the SSI models for each building. The values are normalized by $1/2\rho V$ to get the destructive signal energy for a more convenient display. The energy in the shaking direction is reduced by 3% for structure **E**, **D**, and **A**. Conversely, **B** shows 108% increased energy in this direction, which can be expected as only this structure has a notable increase in ER_{total}. SCI affects building responses orthogonal to the shaking direction more notably. The reason for this is that the trapped waves and reflections from misaligned foundations generate significant excess motion in this direction. Despite the reduced 'x' directional energy in both **E** and **A**, their ER_{total} is slightly increased due to the contribution of excess 'y' and 'z' energy.

4 Discussion and conclusion

The conventional seismic design assumes that buildings are standalone structures, or it occasionally considers interaction with their immediate neighbors using equivalent static approaches. However, complex interactions due to the 3D layout of structures cannot be captured unless the entirety of a building cluster is considered during design. The goal of this study was to assess the combined effects of underground structures and super-tall
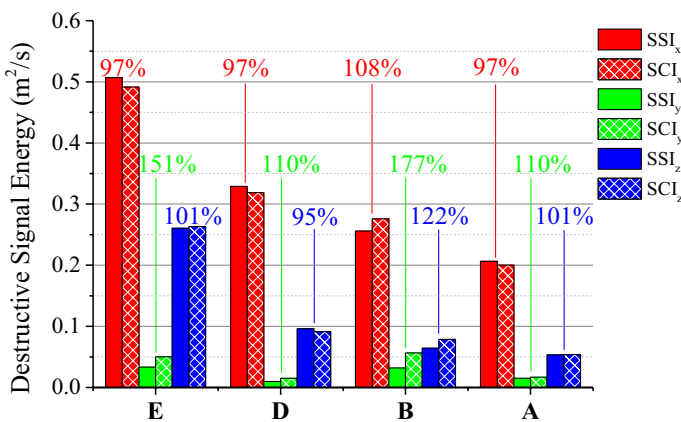

Fig. 17 Destructive signal energy and energy ratios (ER) based on 'x', 'y', and 'z' velocity for structures E, D, B, and A

aboveground structures in a realistic 3D setting. The results presented in this case study call for the consideration of the built environment when designing earthquake-resilient structures at congested urban sites. The fully integrated 3D simulation revealed that surface waves get trapped in the soil enclosed by underground structures due to the 3D interaction between them. Radiation damping is significantly hindered by the presence of neighboring buildings, which act as obstacles and reflect the radiating wave field. Hence, conventional spring and dashpot SSI models may overestimate high-frequency soil damping for a structure in an aggregate with a center plaza layout. To account for the dynamic effect of SCI, it may be necessary to revisit the choice of dynamic impedances used in convectional dashpot and spring SSI models for the design of buildings in an aggregate.

The analysis of SCI effects showed that closely built high-rise buildings can increase each other's seismic demand by interacting via the soil. In terms of structural design, the implications of SCI effects are mostly on serviceability, building content loss, and increased local damage potential. Inter-story drift ratios and maximum relative story displacements of super-tall buildings are not affected notably. On the other hand, closely built super-tall buildings can considerably increase each other's maximum relative story accelerations (MSA). We found that, on average, MSA will increase by 25% in the analyzed structures. Hence, we suggest increasing the MSA calculated from a stand-alone building model by a 1.25 factor to account for SCI effects in congested urban environments. Please note that the heights of the buildings modeled in this study ranged from 50 to 110 stories.

SCI of super-tall buildings severely affects the ground motion in the short period range (0.01–0.3 s). This study shows that PGA increases by up to 20% as far as 300 m outside the building cluster, while wave trapping inside the plaza increases PGA by up to 50%. Therefore, for 3-story and shorter buildings constructed in the vicinity of super-tall building clusters, such as auxiliary buildings, storage facilities, shopping booths, footbridges, etc., we suggest increasing the design PGA by 50% (in a center plaza) or 20% (in the outskirt) to account for the SCI effect. The testbed is located at the water front (Victoria Harbor), hence there is a potential risk for liquefaction in the top fill layers under strong earthquake shaking. The SCI effects may influence the buildup of pore water pressure, thus studies based on a free-field response may underestimate the liquefaction potential. We would like to note that the guidelines discussed herein are based on the case study of some specific high-rise buildings in Hong Kong. This study is intended for moderate to low seismicity area, and a linear behavior of the soil is used in the analysis with adjustment of soil stiffness and damping. For large seismic events, soil nonlinearity needs to be simulated. For a globally applicable guideline, additional and parameterized models need to be considered to validate or alter the suggestions outlined in this paper for different scenarios.

Regarding the effects of SCI on site response the following conclusions are drawn from our study:

- The SCI simulation revealed a significant interaction between underground structures, where surface waves get trapped in the soil enclosed by underground structures. This can lead to constructive wave interference and significant ground motion amplification. In the center plaza and the close outskirts, PGA amplification factors range between 1.2 and 1.5.
- In the case of buildings modeled in isolation (SSI models) energy dissipation mainly happens through radiation damping. However, in the case of an aggregate of buildings (SCI models) radiation damping can be significantly hindered by the presence of neighboring buildings.

- There is a significant passive SCI effect in play, which is a primary cause for notable perturbations in the outskirts of the hub. Super-tall buildings cause the pinning of their surrounding soil via their deep foundations due to their tremendous inertia.
- The building layout was proven to be a defining factor in wave trapping between underground structures and in generating up to $3.5\,m/s^2$ excess demand orthogonal to the shaking direction due to foundations misaligned with the shaking direction.
- SCI drastically decreases ground motion coherency at the site.
- The amplification effects (up to 150-200%) of SCI were only detected in the short period range (0.01-0.3 s) of the acceleration spectra, these periods are further reflected in PGA amplification patterns and the structural responses as well.

By contrasting the standalone reaction of buildings to their reaction in a building cluster, SCI effects were isolated and quantified. We made the following observations regarding the effects of SCI on structural responses:

- As SCI mainly affects the short-period structural responses, while the flexible behavior of tall buildings is mainly controlled by long-period motion, the flexural responses are not altered substantially due to SCI.
- The short period waves amplified through SCI have a significantly adverse effect on the maximum relative story accelerations (MSA). Nearly all floors suffer $1-2\,m/s^2$ excess MSA in 'y' direction, while numerous floors suffer $1\,m/s^2$ additional excitation in 'x'.
- Increased kinetic energy bands repeat in about every 30 m. These bands cover 3–6 floors where the buildings would suffer a 10–20% increase in destructive energy. The repeating pattern can be associated with the high-mode structural response due to increased high-frequency spectral accelerations from the SCI effect. The maximum increase in total kinetic energy (118%) is observed in structure **B**, which is surrounded by a soil zone with high-energy amplification.

In conclusion, the most alarming consequence of SCI on the high-rise is the significant increase in MSA. Furthermore, in the neighborhood of high-rise buildings, SCI effects may significantly increase the demand on short structures ($\leq$3 stories). At developments built with a special layout, such as buildings surrounding a center plaza, wave trapping can adversely affect secondary and interim structures in the plaza. Therefore, we suggest using multiplying factors for PGA and MSA to account for SCI effects during dynamic structural analysis. We would like to note that the current analysis is a case study and uses a single, unidirectional ground motion. Multi-directional shaking and more ground motions will be used in our future studies to provide more robust and generalized findings. Further case studies should also be conducted to help large cities located in seismic zones enhance strategies in financial and insurance policies as well as urban planning.

Declarations

Conflict of interest All authors declare that they have no conflict of interest.

References

Antonietti PF, Mazzieri I, Quarteroni A, Rapetti F (2012) Non-conforming high order approximations of the elastodynamics equation. Comput Methods Appl Mech Eng 209:212–238

Apsel RJ, Luco JE (1987) Impedance functions for foundations embedded in a layered medium: an integral equation approach. Earthq Eng Struct Dyn 15:213–231

ARUP (2015) Seismic hazard analysis of the Hong Kong region. Tech. Rep. GEO-311, Hong Kong SAR

Bard PY, Guéguen P, Wirgin A (1996) A note on the seismic wavefield radiated from large building structures into soft soils. In: Eleventh world conference on earthquake engineering, Acapulco 23-28 June, 1996

Bard P, Chazelas J, Guéguen P, Kham M, Semblat J (2006) Site–city interaction. In: Assess Management Earthquake Risk, pp 91–114

Chaljub E, Moczo P, Tsuno S, Bard PY, Kristek J, Käser M, Stupazzini M, Kristekova M (2010) Quantitative comparison of four numerical predictions of 3D ground motion in the Grenoble Valley, France. Bull Seismol Soc Am 100:1427–1455

Chandler AM, Su R (2007) Dynamic soil properties of Hong Kong reclamation sites for seismic applications. HKIE Trans 7:13–27

Chen Q, Li W (2015) Effects of a group of high-rise structures on ground motions under seismic excitation. Shock Vib 821750

Feng K, Huang D, Wang G, Jin F, Chen Z (2022) Physics-based large-deformation analysis of coseismic landslides: a multiscale 3D SEM-MPM framework with application to the Hongshiyan landslide. Eng Geol (in press)

Graves RW (1996) Simulating seismic wave propagation in 3D elastic media using staggered-grid finite differences. Bull Seismol Soc Am 86:1091–1106

Gu X (2012) Dynamic properties of granular materials at the macro and microscales. Dissertation, University of Hong Kong

Guéguen P, Bard P (2005) Soil–structure and soil–structure–soil interaction: experimental evidence at the Volvi test site. J Earthq Eng 9:657–693

Guéguen P, Bard P, Chávez-García FJ (2002) Site–city seismic interaction in Mexico City-Like environments: an analytical study. Bull Seismol Soc Am 92:794–811

He CH, Wang JT, Zhang CH, Jin F (2015) Simulation of broadband seismic ground motions at dam canyons by using a deterministic numerical approach. Soil Dyn Earthq Eng 76:136–144

Hong Kong Buildings Department (HKBD) (2019) Building records access and viewing on-line. https://bravo.bd.gov.hk/login?request_locale=en_US. Accessed 26 Jan 2021

Housner GW (1957) Interaction of building and ground during an earthquake. Bull Seismol Soc Am 47:179–186

Huang D, Wang G, Du C, Jin F, Feng K, Chen Z (2020) An integrated SEM-Newmark model for physics-based regional coseismic landslide assessment. Soil Dyn Earthq Eng 132:106066

Huang D, Sun P, Jin F, Du C (2021) Topographic amplification of ground motions incorporating uncertainty in subsurface soils with extensive geological borehole data. Soil Dyn Earthq Eng 141:106441

Idriss IM, Sun JI (1993) User's manual for SHAKE91: A computer program for conducting equivalent linear seismic response analyses of horizontally layered soil deposits. Center for Geotechnical Modeling, Davis

Infantino M, Mazzieri I, Özcebe AO, Paolucci R, Stupazzini M (2020) 3D Physics-based numerical simulations of ground motion in Istanbul from earthquakes along the Marmara segment of the North Anatolian fault. Bull Seismol Soc Am 110(5):2559–2576

Isbiliroglu Y, Taborda R, Bielak J (2015) Coupled soil-structure interaction effects of building clusters during earthquakes. Earthq Spectra 31:463–500

Kato B, Wang G (2019) Fully integrated 3D analysis on site–city interaction in an urban transport hub. In: IACGE 2018: Geotechnical and Seismic Research and Practices for Sustainability. ASCE, Reston, pp 312–325

Kato B, Wang G (2021) Regional seismic responses of shallow basins incorporating site-city interaction analyses on high-rise building clusters. Earthq Eng Struct Dyn 50:214–236

Kham M, Semblat J, Bard P, Dangla P (2006) Seismic site–city interaction: main governing phenomena through simplified numerical models. Bull Seismol Soc Am 96:1934–1951

Lin H, Roesset JM, Tassoulas JL (1987) Dynamic interaction between adjacent foundations. Earthq Eng Struct Dyn 15:323–343

Lu X, Tian Y, Wang G, Huang D (2018) A numerical coupling scheme for nonlinear time history analysis of buildings on a regional scale considering site–city interaction effects. Earthq Eng Struct Dyn 47:2708–2725

Luco JE, Contesse L (1973) Dynamic structure–soil–structure interaction. Bull Seismol Soc Am 63:1289–1303

Mason HB, Trombetta NW, Chen Z, Bray JD, Hutchinson TC, Kutter BL (2013) Seismic soil–foundation–structure interaction observed in geotechnical centrifuge experiments. Soil Dyn Earthq Eng 48:162–174

Mazzieri I, Stupazzini M, Guidotti R, Smerzini C (2013) SPEED: Spectral elements in elastodynamics with discontinuous Galerkin: a non-conforming approach for 3D multi-scale problems. Int J Num Meth Eng 95:991–1010

Paolucci R, Mazzieri I, Smerzini C, Stupazzini M (2014) Physics-based earthquake ground shaking scenarios in large urban areas. Perspectives on European earthquake engineering and seismology. Springer, Cham, pp 331–359

Paolucci R, Mazzieri I, Smerzini C (2015) Anatomy of strong ground motion: near-source records and three-dimensional physics-based numerical simulations of the Mw 6.0 2012 May 29 Po Plain earthquake, Italy. Geophys. J Int 203:2001–2020

Pitilakis D, Clouteau D (2010) Equivalent linear substructure approximation of soil–foundation–structure interaction: model presentation and validation. Bull Earthq Eng 8:257–282

Rivière B (2008) Discontinuous Galerkin methods for solving elliptic and parabolic equations: theory and implementation. Soc Ind Appl Math

Sahar D, Narayan JP, Kumar N (2015) Study of role of basin shape in the site–city interaction effects on the ground motion characteristics. Nat Haz 75:1167–1186

Sarrazin MA (1970) Soil–structure interaction in earthquake resistant design. School of Engineering, Massachusetts Institute of Technology, Cambridge

Sarrazin MA, Roesset JM, Whitman RV (1972) Dynamic soil–structure interaction. J Struct Div 98

Schwan L, Boutin C, Padrón LA, Dietz MS, Bard PY, Taylor C (2016) Site–city interaction: theoretical, numerical and experimental crossed-analysis. Geophys J Int 205:1006–1031

Semblat JF, Kham M, Bard PY (2008) Seismic-wave propagation in alluvial basins and influence of site-city interaction. Bull Seismol Soc Am 98(6):2665–2678

Stacey R (1988) Improved transparent boundary formulations for the elastic-wave equation. Bull Seismol Soc Am 78:2089–2097

Taborda R, Bielak J (2011) Full 3D integration of site-city effects in regional scale earthquake simulations. In: Eighth International Conference on Structural Dynamics EURODYN, 4-6 July, 2011, Leuven

Taborda R, Bielak J (2011) Large-scale earthquake simulation: computational seismology and complex engineering systems. Comput Sci Eng 13:14–27

Tsinidis G (2018) Response of urban single and twin circular tunnels subjected to transversal ground seismic shaking. Tunn Undergr Space Technol 76:177–193

Uenishi K (2010) The town effect: dynamic interaction between a group of structures and waves in the ground. Rock Mech Rock Eng 43:811–819

Uenishi K (2013) "Unexpected" failure patterns and dynamic collective behavior of an assembly of buildings subjected to horizontal impact. Eng Fail Anal 35:125–132

Varone C, Lenti L, Martino S, Semblat JF (2021) Spatial variability of the urban ground motion in a highly heterogeneous site–city configurations. Bull Earthq Eng 19:27–45

Wair BR, DeJong JT, Shantz T (2012) Guidelines for estimation of shear wave velocity profiles. PEER report 2012/08. Pacific Earthquake Engineering Research, Berkley

Wang G, Youngs R, Power M, Li Z (2015) Design ground motion library: an interactive tool for selecting earthquake ground motions. Earthq Spectra 31:617–635

Wang G, Du C, Huang D, Jin F, Koo RCH, Kwan JSH (2018) Parametric models for 3D topographic amplification of ground motions considering subsurface soils. Soil Dyn Earthq Eng 115:41–54